Southern Ocean ventilation drives early deglacial ocean carbon release and CO2 rise

Juan Muglia

jmuglia@cenpat-conicet.gob.ar

CONICET https://orcid.org/0000-0002-6968-7723

Andreas Schmittner

Oregon State University https://orcid.org/0000-0002-8376-0843

Stefan Mulitza

MARUM - Center for Marine Environmental Sciences, University of Bremen https://orcid.org/0000-0002-3842-1447

Patrick Rafter

University of South Florida

Janne Repschläger

MPI for Chemistry https://orcid.org/0000-0002-6885-2280

Christopher Somes

GEOMAR Helmholtz Centre for Ocean Research Kiel https://orcid.org/0000-0003-2635-7617

Sophie-Berenice Wilmes

Bangor University https://orcid.org/0000-0002-9174-6910

Article

Keywords: Deglaciation, Carbon, Ocean, Ventilation

Posted Date: September 26th, 2025

DOI: https://doi.org/10.21203/rs.3.rs-7491197/v1

Additional Declarations: There is **NO** Competing Interest.

Southern Ocean ventilation drives early deglacial ocean carbon release and CO_2 rise

Juan Muglia[1,2*], Andreas Schmittner[3], Stefan Mulitza[4], Patrick A. Rafter[5], Janne Repschläger[6], Christopher Somes[7], Sophie-Berenice Wilmes[8]

[1*]Centro para el Estudio de los Sistemas Marinos, CONICET, Bv. Almte Brown 2915, Puerto Madryn, 9120, Chubut, Argentina.
[2*]Universidad Nacional de la Patagonia San Juan Bosco, Bv. Almte Brown 3051, Puerto Madryn, 9120, Chubut, Argentina.
[3]College of Earth, Ocean, and Atmospheric Sciences, Oregon State University, 101 SW 26th St, Corvallis, 97331, Oregon, USA.
[4]MARUM - Center for Marine Environmental Sciences, University of Bremen, Leobener Str. 8, Bremen, 28359, Germany.
[5]College of Marine Science, University of South Florida, 830 1st St S, St. Petersburg, 33701, Florida, USA.
[6]Department of Climate Geochemistry, Max Planck Institute for Chemistry, Hahn-Meitner Weg 1, Mainz, 55128, Germany.
[7]GEOMAR Helmholtz Centre for Ocean Research, Wischhofstr. 1-3, Kiel, 24148, Germany.
[8]School of Ocean Sciences, University of Bangor, Menai Bridge LL59 5AB, Bangor, UK.

*Corresponding author(s). E-mail(s): jmuglia@cenpat-conicet.gob.ar;

Abstract

The early last deglaciation (20-15 ka) is characterized by sea level and atmospheric CO_2 increase. Changes in Atlantic deep water mass structure, Southern Ocean (SO) ventilation, warming ocean temperatures and sinking of organic carbon (export production) are suggested to transfer carbon from the ocean to the atmosphere. However, quantification of those processes is complex due to rapid deglacial dynamics and uncertainties of forcings and feedbacks involved. Here we analyze a global compilation of stable carbon isotope ratios ($^{13}C/^{12}C$) from benthic foraminifera, which shows enrichment in deep waters of Antarctic origin, and depletion in upper North Atlantic Deep Waters during Heinrich Stadial 1. We test, using the glacial configuration of a global climate model, the effect on the carbon cycle of three deglacial forcings: North Atlantic fresh water fluxes (FWF), increased SO ventilation, and lower atmospheric iron fluxes. We find that increased SO ventilation and reduced iron fluxes increase SO $^{13}C/^{12}C$ of dissolved inorganic carbon (DIC), which propagates to Indo-Pacific and lower Atlantic deep waters, in agreement with reconstructions, while inferred changes in the Atlantic Meridional Overturning Circulation (AMOC) are small. Combining all forcings, our simulations are able to reproduce the early deglacial CO_2 rise.

Keywords: Deglaciation, Carbon, Ocean, Ventilation

Despite contributing importantly to global temperature variations during glacial cycles[1], changes in atmospheric CO_2 are not well understood. They have been attributed to changes in deep ocean carbon[2], modulated by temperature, sea ice, a redistribution of deep water masses, ventilation, and sequestration of biological carbon[3–9]. Here we focus on the early last deglacation, which provides a wealth of well-dated reconstructions, and is associated with a $\sim$33 ppm[10] CO_2 rise.

FWF from melting of the Laurentide and European ice sheets[11] have been suggested to slow down the AMOC[12, 13] during Heinrich Stadial 1 (HS1, 16.5–15.0 ka). This is indicated by paleotracers such as decreasing $^{13}C/^{12}C$ ratios ($\delta^{13}C$ when compared with a standard) in upper North Atlantic Deep Water (NADW)[14, 15]. However, quantifying AMOC changes remains challenging and their role on atmospheric CO_2 is still unclear[4, 13, 16, 17].

Lower atmospheric iron deposition via dust could have hampered SO productivity and transfer of carbon from the surface to the deep ocean, resulting in atmospheric CO_2 increase after the Last Glacial Maximum (LGM, 22-20 ka)[3, 18]. On the other hand, reinvigorated SO ventilation, driven by poleward shifts and/or intensification of Southern Hemisphere Westerlies, could have decreased the isolation of Antarctic-sourced deep waters and released deep ocean carbon into the atmosphere[4, 7, 8, 19].

$\delta^{13}C$ in tests of benthic foraminifera *C. wuellerstorfi* have been used as a proxy for deep water mass distribution[20], though changes in the source waters $\delta^{13}C$ and organic matter remineralization have to be considered[15, 21]. A new compilation of high resolution (> 1 ka) downcore *C. wuellerstorfi* stable isotope measurements from deglacial sediments[22] provides an unprecedented opportunity to reconstruct changes in deep water mass distribution[23]. Here we analyze this data base with transient simulations of an intermediate-complexity, isotope-enabled Earth-System Model with interactive carbon cycle, to help interpret the observations. We assess effects of FWF, enhanced wind-driven SO ventilation, and export production reduction (Fig. S1) on atmospheric CO_2, $\delta^{13}C_{CO_2}$, and deep water $\delta^{13}C$. The simulated $\delta^{13}C$ is subsampled to match locations and ages of the observations. This four-dimensional approach dispenses of defining time intervals, which can add extra uncertainties in a model-data comparison. It allows the use of all data points corresponding to the early last deglaciation within a core site, resulting in a sample size of $\sim$ 2000 data points.

Results

Observed changes in deep ocean δ^{13}C

C. wuellerstorfi δ^{13}C data[22] reveal substantial changes between the LGM (22-20 ka) and Heinrich Stadial 1 (HS1, 17-15 ka) (Fig. 1). δ^{13}C increases in deep waters of Antarctic origin, propagating a $0.1 - 0.3$ permil increase to most of the Indo-Pacific Ocean and to Antarctic Bottom Water (AABW) in the Atlantic (Fig. 1), a pattern that has not been described before. Upper NADW (Atlantic Ocean above 2500 m) exhibits a $0.1 - 0.3$ permil δ^{13}C decrease, with negative anomalies as high as 0.6 permil in Arctic waters between 1000 and 2000 m (Fig. 1). In the Atlantic Ocean, the result is a "dipole effect" between upper waters and lower waters, which tends to reduce the vertical gradient of $\delta^{13}C_{DIC}$.

Modeled ocean physics

Simulations with FWF forcings decrease AMOC transport and shoal the interface between the AMOC and AABW overturning cells (AMOC depth hereafter). A North Atlantic FWF of 0.053 Sv between 20 and 15 ka (Fig. S1) decreases the AMOC transport at 25° N from 13 to 9 Sv (**LFWF**, Fig. 2a), and decreases its depth from 2700 to 2400 m (Fig. 2b). Increasing FWF from 0.056 to 0.087 Sv at 17 ka, following reconstructed volume equivalent sea level changes[11], produces a gradual AMOC shut down (**HFWF**).

Higher SO ventilation from a gradual wind stress intensification (Figs. S1, S2), on the other hand, increases AMOC transport to 15 Sv in the **SOWind** and **SOWind_LDust** simulations (Fig. 2a). Thus, a decrease in AMOC transport by North Atlantic FWF may be moderated by higher SO ventilation. For example, the combined experiment **LFWF_SOWind_LDust** gives an AMOC of 11 Sv and 2500 m depth, slightly weaker than the modeled LGM. Most importantly, increased SO ventilation may work to stabilize the AMOC upon high North Atlantic FWF. For instance, **HFWF_SOWind_LDust** exhibits an active AMOC of 8 Sv and 2400 m, as opposed to the collapsed circulation of **HFWF** (Fig. 2a,b).

Atmospheric tracers

An AMOC weakening decreases modeled atmospheric CO_2 by 6-9 ppm (Fig. 2c), as it increases deep ocean carbon storage due to a more sluggish circulation and more expansive AABW. In contrast, a gradual 85 % decrease in SO dust flux between 20 and 15 ka (Fig. S1), consistent with dust flux estimates from ice core data[3], lowers SO export production and remineralization in the deep ocean, and produces a gradual CO_2 increase of 30 ppm (**LDust**, Fig. 2c). This represents 80 % of the CO_2 change between 20 and 15 ka BP reconstructed from Antarctic ice cores[10], which suggests that lower dust was the major driver of the initial deglacial CO_2 incease.

Higher SO ventilation releases deep carbon to the atmosphere, further increasing CO_2 by 14 ppm (**SOWind_LDust**, Fig. 2c). **LFWF_SOWind_LDust** and **HFWF_SOWind_LDust** exhibit the highest resemblance between modeled and reconstructed CO_2 curves between 20 and 15 ka, with atmospheric CO_2 increasing

33 ppm by 15 ka. These experiments also show the best model-data agreement with atmospheric $\delta^{13}C_{CO_2}$ reconstructions[24] between 20 and 16 ka (Fig. 2d), although some rapid $\delta^{13}C_{CO_2}$ changes are not reproduced.

Deep ocean model-data comparison

Our simulations suggest that SO processes may explain the vertical gradient decrease in Atlantic δ^{13}C observations between the LGM and HS1 (Fig. 3a). Higher SO ventilation and lower atmospheric iron flux increase δ^{13}C in the Indo-Pacific Ocean, and in the Atlantic Ocean below 2500 m south of 35° N (Fig. S3). On the other hand, North Atlantic FWF leads to a decrease of deep ocean δ^{13}C in most regions, which does not agree with reconstructed HS1-LGM changes (Figs. 3a, S3).

The correlation (R), normalized root mean square error (RMSE), and slope of modeled versus data δ^{13}C can be used to asses the most likely combination of forcings that explains the observed data (see Methods). Higher ventilation improves δ^{13}C model-data agreement, reflected by simulations with higher R, lower RMSE, and slopes closer to 1 (Table 1). The metrics are also improved when North Atlantic FWF are applied (**LFWF**), which produce a stable AMOC that is weaker and shallower than in **Control**. However, a collapsed AMOC as a result of high freshwater fluxes (**HFWF**)[11], does not agree well with deglacial δ^{13}C data (Table 1, Fig. 3). Combining SO ventilation, SO iron flux, and North Atlantic FWF forcings produces the best model-data agreement (**LFWF_SOWind_LDust**, **HFWF_SOWind_LDust**, see Table 1).

Discussion

HS1-LGM differences

A southward shift and strengthening of the Southern Hemisphere Westerlies increases SO ventilation and all southern-sourced deep waters, as illustrated by higher dissolved oxygen levels in simulations that include that forcing (Fig. S4). In the Atlantic, models with higher SO ventilation reproduce the observed early deglacial reduction of vertical δ^{13}C gradient (Fig. 3a-b). In the Southern and Indo-Pacific Oceans, the reconstructed early deglacial δ^{13}C raise is associated with higher ventilation, as evidenced by the agreement between modeled and observed time series when that forcing is applied (Fig. 3c-d). Lower atmospheric iron fluxes further increase agreement between model and observations (orange dashed-dotted lines in Fig. 3). Simulations that include only North Atlantic FWF exhibit lower δ^{13}C values in most of the Atlantic water column (light and dark blue solid lines in Fig. 3), in disagreement with observations. Indo-Pacific section plots show that our simulations predict LGM to HS1 changes of opposite sign than the data unless SO forcings are applied (Fig. S3).

Physical and biogeochemical processes

Section and profile plots show that higher SO ventilation and lower export production increase δ^{13}C in waters of Antarctic origin (Fig. 3). These processes oxygenate the deep ocean (Fig. S4) and induce a transfer of carbon to the atmosphere from the SO (Fig. S5), which raises atmospheric CO_2 concentration (Fig. 2c). Ventilation has a more limited effect on atmospheric CO_2 than export production decrease (dashed line in Fig. 2c). This suggests that while SO ventilation is necessary to reproduce early deglacial increase in $\delta^{13}C$ values in AABW and Indo-Pacific Waters found in sediment core data, an export production decrease is necessary to reproduce observed atmospheric CO_2 changes.

Radiocarbon ages, which are mostly affected by physics[7], show that an increase in SO ventilation produces younger waters in the South Atlantic and Pacific Oceans (Fig. S6). This may explain reconstructions from downcore benthic foraminifera[25], which in the SO show negative anomalies between HS1 and LGM. On the other hand North Atlantic FWF, which reduces AMOC transport and depth (Fig. 2), may explain observations of older NADW during HS1[25] (Fig. S6). Model-data agreement improves when higher SO ventilation is included in the simulations, as evidenced by the higher R and lower RMSE (Table S1).

Dynamical analysis of the early last deglacation

Considering all global $\delta^{13}C$ data between 20 and 15 ka BP (Fig. 1) and the co-located model output, shows that increased SO ventilation produces data-model pairs with regression lines closer to the 1:1 line (Fig. S7) in the **SOWind_Ldust**, **LFWF_SOWind_Ldust**, and **HFWF_SOWind_Ldust** simulations (Table 1). Modeled time series of mean $\delta^{13}C$ differences between the upper and lower Atlantic (Fig. 3b), as well as modeled HS1 minus LGM mean vertical profile changes (Fig. 3a), illustrate that the deglacial decrease in the Atlantic $\delta^{13}C$ vertical gradient is driven by processes that increase SO $\delta^{13}C$ and propagate that signal to all Antarctic-originated water masses (Fig. 3c-d). The four dimensional analysis (Table 1, Fig. S7) indicates that simulations that combine SO (ventilation, iron fluxes) and North Atlantic FWF forcings give the best representation of deglacial $\delta^{13}C$ data between 20 and 15 ka. A 5° poleward shift and strengthening of the Westerlies over the SO (Fig. S5), as suggested by a combination of planktic foraminiferal $\delta^{18}O$ and climate models[6], and opal flux reconstructions[26], increases SO ventilation and oxygenates Antarctic waters (Fig. S4), increasing $\delta^{13}C$. This propagates young, $\delta^{13}C$-enriched waters to the deep Indo-Pacific Ocean and to the lower Atlantic Ocean (Fig. S3).

Reconstructions of deep ocean $\delta^{13}C$ changes between HS1 and the LGM[22] exhibit higher values in Indo-Pacific Deep Waters and AABW, and lower values in upper NADW (Fig. 1). Our model results suggest that higher ventilation and a reduction in atmospheric iron flux (as suggested by ice core reconstructions[3, 27]) explain those observations. Combining lower atmospheric iron flux with higher SO ventilation we are also able to reproduce LGM to HS1 changes in atmospheric CO_2 (Fig. 2), consistent with previous hypotheses[7, 8].

Drivers of the HS1 atmospheric-ocean carbon exchange

Our results suggest that higher SO ventilation oxygenate the deep ocean and induce the early deglacial $\delta^{13}C$ increase measured in *C. wuellerstorfi* in the Indo-Pacific Ocean and below 2500 m in the Atlantic Ocean. They agree with previous modeling studies that addressed the effects of wind stress on glacial-interglacial atmospheric CO_2

differences[4, 5, 19], although ventilation could also have been increased by buoyancy fluxes[28]. The inclusion of North Atlantic FWF to the simulations improves the model-data agreement, as **LFWF_SOWind_Ldust** and **HFWF_SOWind_Ldust** give the best comparison metrics among our simulations (Table 1). AMOC shoaling produces a negative δ^{13}C anomaly at the NADW/AABW interface where the vertical gradients are strong, although the model's LGM AMOC and thus the δ^{13}C front is likely too deep (Fig. S11) in our simulations. Whereas in the observations the δ^{13}C minimum is around 2000 m depth, in the model it is around 4000 m depth (Fig. S3). Thus our simulations are not conclusive in the effects of North Atlantic FWF and AMOC transport in setting up early deglacial deep ocean carbon changes, but agree with multi-proxy model-data comparison studies that suggest an active HS1 AMOC[16, 21, 29].

We conclude that the most likely early deglacial deep water scenario is one where the AMOC is active but shallower than in the LGM (Fig. 4). Increased ventilation in Antarctic waters results in oxygenation of Antarctic-sourced Atlantic and Indo-Pacific Deep Waters. Deep ocean δ^{13}C increases in those water masses (Fig. 4) accompanied by a rise in atmospheric CO_2 and a decrease in $\delta^{13}C_{CO_2}$ between 20 and 15 ka (Fig. 2). North Atlantic FWF induce older NADW, with lower values of δ^{13}C than in the LGM. The resulting state agrees with most LGM to HS1 δ^{13}C differences captured by deep ocean sediment core data (Fig. 4c), and simultanously explains the transfer of carbon to the atmosphere that leads to the observed CO_2 increase.

Methods

The model

For model simulations we use the global ocean intermediate complexity model of the University of Victoria (UVic)[30], version 2.9. Its ocean component consists of a $3.6° \times 1.8°$ horizontal resolution grid and 19 vertical levels governed by the primitive equations. Vertical and isopycnal diffusivities are parametrized, and tidal energy dissipation uses a prescribed sub-grid bathymetry[31]. UVic includes a dynamic-thermodynamic sea ice model, which accounts for changes in surface salinity[32], and a two-dimensional energy-moisture balance atmospheric model which calculates surface air temperatures and moisture but uses prescribed wind fields. It is also coupled with a dynamic land vegetation model[33].

UVic is equipped with the Model of Ocean Biogeochemistry and Isotopes (MOBI) that includes prognostic nutrients (PO_4, NO_3, Fe, Si), different functional types of phytoplankton (phytoplankton, diazotrophs, diatoms), as well as zooplankton, detritus, and particulate iron. It also includes organic nitrogen and phosphorous, and variable iron-binding ligands[34–36]. The model includes interactive carbon isotope cycles, which allows one-to-one comparisons between model output and paleotracer reconstructions.

LGM initial state

The LGM simulation used as initial condition for our deglaciation experiments includes LGM orbital forcings and atmospheric CO_2 set constant at 189.7 ppm. The ICE6G-C land ice sheet reconstruction[37] corresponding to 20 ka BP is applied to the continental orography and is used to calculate the LGM bathymetry for tidal energy dissipation[31].

As in previous works[38], we apply a 40% decrease on SH meridional moisture diffusivity to account for decreased meridional moisture transport under colder conditions[39], a 0.08 Sv negative fresh water flux anomaly over the North Atlantic Ocean, and a +1 PSU global salinity anomaly to account for LGM minus Holocene sea level differences. Northern Hemisphere wind stress fields are modified with LGM minus Late Holocene anomalies calculated from Paleoclimate Model Intercomparison Project models[40]. Because in this work we are interested in the effect of early deglacial changes in winds over the SO, for the LGM simulation the region of maximum strength of the Westerlies in the Southern Hemisphere is extended 5° equatorward with respect to wind fields used in previous works (Fig. S2).

For the biogeochemical component of the model, in the LGM simulations sedimentary iron fluxes are increased with respect to the preindustrial, accounting for lower sea level and more exposed continental shelves[41]. A reconstruction of LGM surface atmospheric dust fluxes is used for surface surface soluble iron fluxes[42], including a $x10$ increase over the SO[41].

This combination of boundary conditions produces a meridional overturning configuration that can be described as "intermediate-shallow"[38], with an interface between the AMOC and AABW cells at depth 2600 ± 200 m and a maximum AMOC transport at 25° N of 13 Sv (Fig. S8). For comparison, a preindustrial simulation in UVic exhibits an AMOC interface of 3000 ± 200 m depth and maximum AMOC transport at 25° N of 17 Sv. AABW and lower NADW occupy a higher portion of the Atlantic Ocean and are less ventilated in the LGM simulation than in the preindustrial, as can be seen in basin zonal means of dissolved O_2 (Fig. S9). The core of glacial upper NADW, identified with the 0.24 mol/m^3 isoline, becomes 700 m shallower in the LGM compared with the preindustrial simulation. The Indo-Paficic also exhibits lower ventilation, with lower dissolved O_2 values in most of its volume. Zonal mean δ^{13}C of DIC (Fig. S10) exhibits lower isotope rations in AABW and lower glacial NADW in the LGM simulation, accounting for higher isolation due to extended winter sea ice in both hemispheres, as well as higher SO EP[38]. The interface between upper glacial NADW and AABW/lower glacial NADW is pushed upwards in the water column, as suggested by most reconstructions based on δ^{13}C of benthic foraminifera in sediment cores[20, 43].

δ^{13}C of DIC in our LGM simulation shows a deep water mass structure similar to results from a recent global compilation of δ^{13}C of *C. wuellerstorfi* reconstructions[22] in the general pattern, yet sight differences are observed. To quantify the model and data discrepancies, we first transform modeled δ^{13}C of DIC into δ^{13}C of *C. wuellerstorfi* using a core top calibration[44]. We normalize the model minus data δ^{13}C at each core site with the combined model and data LGM minus Late Holocene global δ^{13}C difference (calculated by error propagation methods to be 0.54 permil). The time slice from the global compilation used for the model-data comparison is $22-20$ ka BP. Indo-Pacific and South Atlantic Oceans exhibit a good model-data agreement in most sites (Fig. S11), with model-data discrepancies ranging between 0 and 0.3 permil. In the North Atlantic, higher discrepancies occur between 2000 and 3000 m, because of a deeper AABW-upper glacial NADW interfase simulated in the model than predicted by the data (orange-brown colors in Fig. S11e). As a result of this bias, a shoaling of the AMOC in the model leads to δ^{13}C vertical minima that are deeper than in the observations. Nevertheless, modeled end-member NADW and AABW δ^{13}C values are in good agreement with the data.

Deglacial simulations

We assess the individual effects of different forcings on changes in global ocean distribution of δ^{13}C in the 20-15 ka BP interval using different forcing scenarios (Fig. S1).

Control_0 is a continuation between 20 and 15 ka of the LGM simulation.

Control includes transient changes in land ice sheets calculated after the ICE6G-C reconstruction[37], which represent an 8% decrease between 20 and 15 ka BP in the ice sheet volume of the Northern Hemisphere. The effect on the physics of the Global Ocean in a coarse resolution model due to the changes in orography associated with this reduction in the Northern Hemisphere land ice sheets is very limited[45]. We thus use **Control** as the baseline simulation for the rest of deglacial experiments, and will not further discuss differences between **Control** and **Control_0**.

LDust is as **Control** but a gradual reduction in atmospheric iron flux is applied. The reduction was calculated by scaling atmospheric soluble iron flux over the SO with the early last deglaciation decrease on dust flux determined from Antarctic ice cores[3]. This results in a 85 % decrease between 20 and 15 ka (Fig. 4), in line with estimates of deglacial soluble iron flux changes from ice cores[27].

LFWF is as **Control** but surface FWF are applied between 20 and 15 ka in the North Atlantic, North-East Pacific, and SO (around Patagonia), to account for glacier discharge from the melting of land ice sheets. The grid boxes where the fresh water fluxes were applied, as well as the fraction of that flux going into each region, follow a glacier discharge plume map determined from a drainage network model (Fig. S12)[46]. Most (93 %, 0.053 Sv) of that flux goes into the North Atlantic Ocean, and only 10 and 6 % go into the North-East Pacific and Southern Oceans, respectively. The total FWF applied is 0.061 Sv, calculated after an estimate of volume equivalent sea level change during the first 3 ka of the last deglaciation, reconstructed from coral and sediment records[11]. That volume equivalent sea level change reconstruction suggests fresh water fluxes of 0.061 Sv between 20 and 17 ka BP, and of 0.100 Sv between 17 and 15 ka BP. Applying 0.053 Sv between 20 and 15 ka in the **LFWF** simulation functions as a lower limit for the effects of FWF to the deglacial ocean. It produces an AMOC that is weaker and shallower than in **Control**, but is still active (Fig. 2).

HFWF is as **LFWF** but the fresh water forcing is increased to 0.087 Sv between 17 and 15 ka, following estimates of volume equivalent sea level change during that interval[11]. In this case, the transport of the AMOC linearly decreases and collapses by 15 ka BP (Fig. 2).

SOWind is as **Control** but a 5° poleward shift and a gradual strengthening in the zonal wind stress over the SO are applied (Fig. S2). These changes follow qualitative estimates of differences between LGM and Holocene wind stress in sup-polar regions[5, 6]. Some of the Paleoclimate Model Intercomparison Project models, equipped with a three dimensional atmosphere coupled to the ocean component, predict lower wind stress intensity over the SO in their LGM simulations[47]. The wind stress strengthening applied in **SOWind** serves as a way to study the sensitivity of deep ocean tracers to changes in SO ventilation, although ventilation changes could also have been forced by buoyancy fluxes[28].

SOWind_LDust is a combination of the **SOWind** and **LDust** simulations.

LFWF_SOWind_LDust is a combination of the **LFWF** and **SOWind_LDust** simulations.

HFWF_SOWind_LDust is a combination of the **HFWF** and **SOWind_LDust** simulations.

Four-dimensional model-data comparison

We compare the 20-15 ka model output δ^{13}C of DIC from the model simulations with a data base of *Cibicidoides wuellerstorfi* δ^{13}C from globally-distributed deep sea sediment cores[22]. Modeled δ^{13}C of DIC is transformed into *C. wuellerstorfi* δ^{13}C by applying a regression calculated after Late Holocene data[44]. Because of the dynamics of the early last deglaciation, a four dimensional approach is used for the model-data comparison. We extract the model output δ^{13}C of the nearest grid box at each core location, corresponding to the ages given by their downcore age model[22]. This is different to past efforts where a fixed time interval was defined, and a three dimensional model-data comparison was performed inside that interval[38, 48, 49].

To avoid bioturbation issues in the data, we perform the analysis only including sites that have a time resolution higher than 1 ka between 20 and 15 ka BP. The number of samples in the statistical analysis is 2040, much larger than in previous works that used a time slice approach and thus used only one averaged data point per coring site ($\sim 300 - 400$ samples[38]).

We use three different statistical metrics to measure the level of agreement between model and data δ^{13}C in the Global Ocean: Correlation coefficient (R), global bias-corrected root-mean square error (RMSE), and slope of model versus data scatter plot. RMSE is normalized by the combined model and data LGM minus Late Holocene global δ^{13}C difference (0.54 permil). This way, RMSE values smaller than 1 present a model-data disagreement smaller than the estimated glacial-interglacial δ^{13}C difference. The model versus data scatter plot is constructed for each model experiment, using data points between 20-15 ka at all core sites of the δ^{13}C data base (Fig. S7). In a perfect model-data agreement, all points should coincide with the 1:1 line. Thus, simulations with better model-data agreement have slopes closer to 1.

Supplementary information. This article includes Supplementary figures and a table.

Acknowledgements. JM acknowledges CONICET and UNPSJB. AS was supported by the US National Science Foundation. Data compilation was supported by the

Table 1 Summary of deglacial simulations, and results of a four dimensional model-data comparison using downcore *C. wuellerstorfi* δ^{13}C from sites with > 1 ka resolution[22]. RMSE is normalized by the combined model and data LGM minus Late Holocene global δ^{13}C difference (0.54 permil). Slope was calculated from model versus data scatter plots of each simulation (Fig. S7). AMOC and export production were calculated averaging the last 1 ka of simulations. Statistical metrics were calculated for data points between 20 and 15 ka. Offsets in global mean δ^{13}C between simulations and data were removed to calculate de metrics. The final state of the HFWF simulation is a collapsed AMOC.

Simulation	AMOC (Sv)	AMOC depth (m)	EP (Pg C/a)	R	RMSE	Slope
Control	12.7	2672	19.2	0.75	0.74	0.74
Ldust	13.3	2692	18.8	0.76	0.69	0.83
SOWind	14.4	2671	19.3	0.78	0.68	0.82
SOWind_Ldust	15.1	2735	18.3	0.78	0.65	0.91
LFWF	09.2	2437	17.9	0.78	0.69	0.78
HFWF	02.5	1548	16.7	0.68	0.82	0.69
LFWF_SOWind_Ldust	10.7	2551	18.0	0.80	0.63	0.91
HFWF_SOWind_Ldust	07.7	2396	17.7	0.80	0.62	0.93

Past Global Changes (PAGES) working group *Ocean Circulation and Carbon Cycling* (OC3). This work is a product of the project *Proxies of Ocean Circulation and Water Properties: Evaluation, Reconstruction and Simulation* (POWERS).

Conflict of interest. The authors declare no conflict of interest.

Data availability. Model output used to perform the analysis of this paper can be found in the CONICET repository (Argentina): http://hdl.handle.net/11336/267413. The δ^{13}C of downcore benthic foraminifera may be found at https://zenodo.org/records/11187264.

Author contribution. JM designed and ran the computer simulations, performed analysis, and wrote the first version of the paper. CS and SBW provided code and input files for running the simulations. All co-authors provided important ideas and comments for performing the analysis of results and writing of the paper.

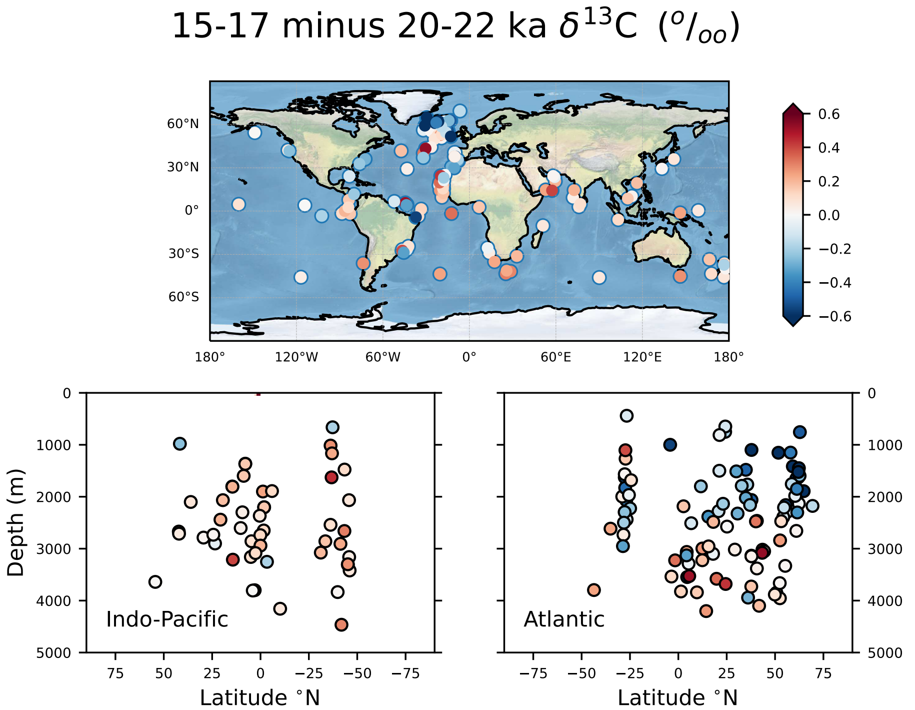

Fig. 1 (top) Coring sites with time resolution higher than 1 ka used in this work[22]. Color scale indicates HS1 minus LGM δ^{13}C differences from *C. wuellerstorfi* tests. (bottom) The same data as in the top panel, but represented as zonally-collapsed sections in (right) the Indo-Pacific and (left) the Atlantic Oceans.

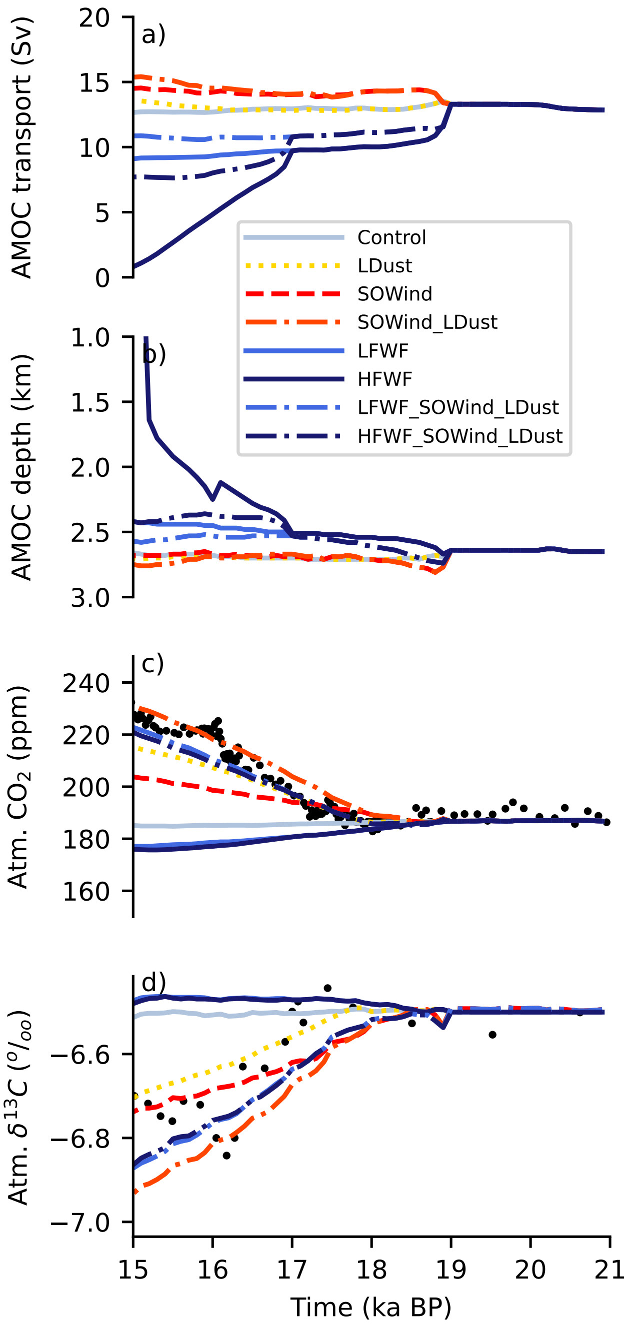

Fig. 2 Time series of maximum AMOC transport at 25° N, mean depth of the interfase between AMOC and AABW cells (25° S - 25° N), and atmospheric CO_2 and δ^{13}C from our simulations. Atmospheric tracer plots include reconstructions from Antarctic ice cores[10, 24].

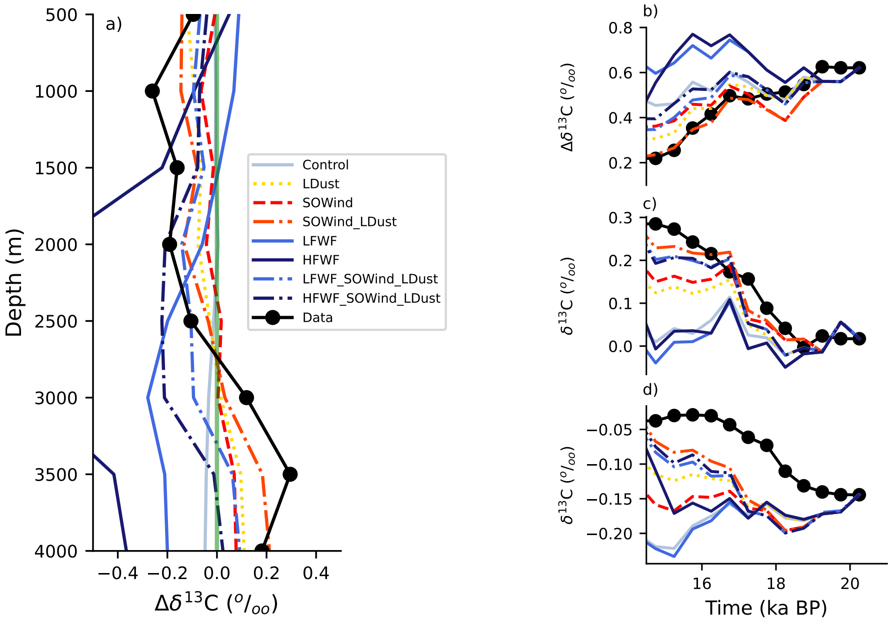

Fig. 3 (a) Atlantic low-latitude (40° S - 40° N) profile plot of zonally- and meridionally-averaged δ^{13}C differences between the $15-17$ and $20-22$ ka time slices from *C. wuellerstorfi* data and our simulation results. Averages calculated from the model output using grid boxes co-located with the data. Data and model output were averaged in 500 m intervals. The zero change line is indicated in green. Results for the **HFWF** simulation lie mostly outside of the plot's horizontal range. (b) Time series of δ^{13}C differences between the upper (< 2500 m) and lower (> 2500m) low-latitude (40° S - 40° N) Atlantic, from *C. wuellerstorfi* data and our simulations results. (c) Time series of δ^{13}C from the SO (south of 30° S), from *C. wuellerstorfi* data and our simulations results. (d) as c), but for Indo-Pacific Ocean. Model means are calculated using grid boxes co-located with the data, and averaged over 0.5 ka intervals. Time series corresponding to the data are smoothed using a 0.5 ka boxcar filter. Time series of model outputs are shifted in order to coincide with the reconstructions at the oldest data point.

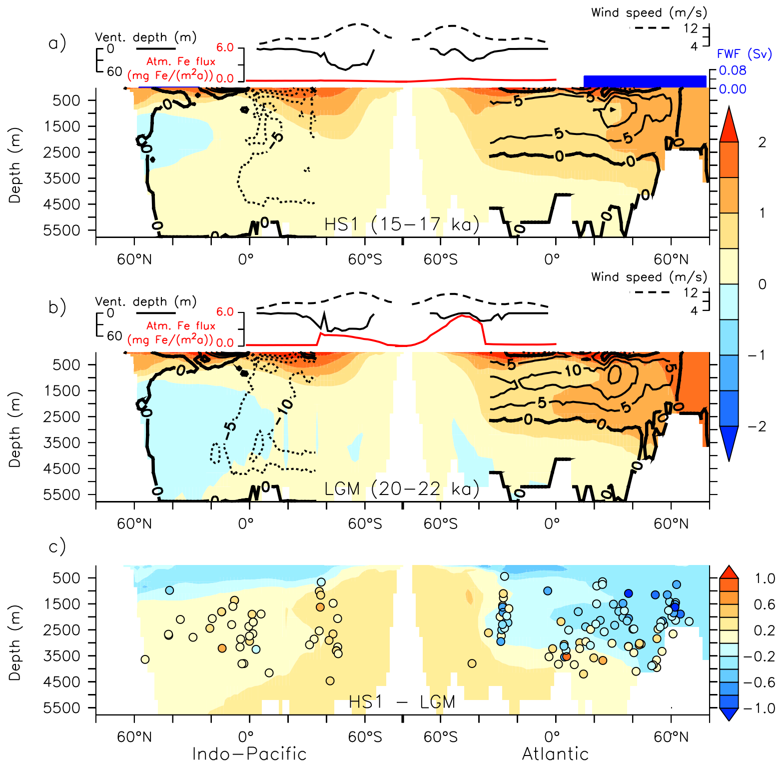

Fig. 4 Modeled (a) HS1 and (b) LGM scenarios, taken from the **LFWF_SOWind_Ldust** simulation. Contours correspond to meridional streamfunction in Sv, and shadings correspond to modeled zonally-averaged δ^{13}C of DIC, transformed into δ^{13}C of *C. wuellerstorfi* by using a core-top calibration[44]. FWF, SHW, and atmospheric Fe fluxes applied at each time slice are included in the plots, as well as SO ventilation depths. (c) Comparison between model output and paleoceanographic data[22]: δ^{13}C differences from the two time slices, with zonally-collapsed data overlayed using the same color scale. The simulation is able to reproduce the strucutre of HS1 minus LGM changes in deep water δ^{13}C in Atlantic and Indo-Pacific ocean basins.

References

[1] Shakun, J. D. *et al.* Global warming preceded by increasing carbon dioxide concentrations during the last deglaciation. *Nature* **484**, 49–54 (2012).

[2] Sigman, D. M. & Boyle, E. A. Glacial/interglacial variations in atmospheric carbon dioxide. *Nature* **407**, 859–869 (2000).

[3] Martínez-García, A. *et al.* Iron fertilization of the Subantarctic Ocean during the last ice age. *Science* **343**, 1347–1350 (2014).

[4] Menviel, L. *et al.* Southern hemisphere westerlies as a driver of the early deglacial atmospheric co2 rise. *Nature Communications* **9**, 2503 (2018).

[5] Sigman, D. M. *et al.* The Southern Ocean during the ice ages: A review of the antarctic surface isolation hypothesis, with comparison to the North Pacific. *Quaternary Science Reviews* **254**, 106732 (2021).

[6] Gray, W. R. *et al.* Poleward shift in the Southern Hemisphere westerly winds synchronous with the deglacial rise in CO2. *Paleoceanography and Paleoclimatology* **38**, e2023PA004666 (2023).

[7] Skinner, L. *et al.* Rejuvenating the ocean: mean ocean radiocarbon, CO2 release, and radiocarbon budget closure across the last deglaciation. *Climate of the Past* **19**, 2177–2202 (2023).

[8] Wendt, K. A. *et al.* Southern Ocean drives multidecadal atmospheric CO2 rise during Heinrich Stadials. *Proceedings of the National Academy of Sciences* **121**, e2319652121 (2024).

[9] Khatiwala, S., Schmittner, A. & Muglia, J. Air-sea disequilibrium enhances ocean carbon storage during glacial periods. *Science advances* **5**, eaaw4981 (2019).

[10] Marcott, S. A. *et al.* Centennial-scale changes in the global carbon cycle during the last deglaciation. *Nature* **514**, 616–619 (2014).

[11] Lambeck, K., Rouby, H., Purcell, A., Sun, Y. & Sambridge, M. Sea level and global ice volumes from the Last Glacial Maximum to the Holocene. *Proceedings of the National Academy of Sciences* **111**, 15296–15303 (2014).

[12] Gherardi, J.-M. *et al.* Glacial-interglacial circulation changes inferred from 231Pa/230Th sedimentary record in the North Atlantic region. *Paleoceanography* **24** (2009).

[13] Schmittner, A. & Lund, D. Early deglacial Atlantic overturning decline and its role in atmospheric CO2 rise inferred from carbon isotopes (δ 13 c). *Climate of the Past* **11**, 135–152 (2015).

[14] Lund, D., Tessin, A., Hoffman, J. & Schmittner, A. Southwest Atlantic water mass evolution during the last deglaciation. *Paleoceanography* **30**, 477–494 (2015).

[15] Blaser, P. *et al.* Prevalent North Atlantic Deep Water during the Last Glacial Maximum and Heinrich Stadial 1. *Nature Geoscience* **18**, 410–416 (2025).

[16] Pöppelmeier, F., Jeltsch-Thömmes, A., Lippold, J., Joos, F. & Stocker, T. F. Multi-proxy constraints on atlantic circulation dynamics since the last ice age. *Nature geoscience* **16**, 349–356 (2023).

[17] Snoll, B. *et al.* A multi-model assessment of the early last deglaciation (PMIP4 LDv1): a meltwater perspective. *Climate of the Past* **20**, 789–815 (2024).

[18] Wang, X. T. *et al.* Deep-sea coral evidence for lower Southern Ocean surface nitrate concentrations during the last ice age. *Proceedings of the National Academy of Sciences* **114**, 3352–3357 (2017).

[19] Toggweiler, J. R., Russell, J. L. & Carson, S. R. Midlatitude westerlies, atmospheric CO2, and climate change during the ice ages. *Paleoceanography* **21** (2006).

[20] Curry, W. B. & Oppo, D. W. Glacial water mass geometry and the distribution of δ13C of ΣCO2 in the western Atlantic Ocean. *Paleoceanography* **20** (2005).

[21] Repschläger, J. *et al.* Active North Atlantic deepwater formation during Heinrich Stadial 1. *Quaternary Science Reviews* **270**, 107145 (2021).

[22] Muglia, J. *et al.* A global synthesis of high-resolution stable isotope data from benthic foraminifera of the last deglaciation. *Scientific Data* **10**, 131 (2023).

[23] Kobayashi, H., Oka, A., Obase, T. & Abe-Ouchi, A. Assessing transient changes in the ocean carbon cycle during the last deglaciation through carbon isotope modeling. *Climate of the Past* **20**, 769–787 (2024).

[24] Bauska, T. K. *et al.* Carbon isotopes characterize rapid changes in atmospheric carbon dioxide during the last deglaciation. *Proceedings of the National Academy of Sciences* **113**, 3465–3470 (2016).

[25] Rafter, P. A. *et al.* Global reorganization of deep-sea circulation and carbon storage after the last ice age. *Science Advances* **8**, eabq5434 (2022).

[26] Anderson, R. *et al.* Wind-driven upwelling in the Southern Ocean and the deglacial rise in atmospheric CO2. *science* **323**, 1443–1448 (2009).

[27] Conway, T., Wolff, E., Röthlisberger, R., Mulvaney, R. & Elderfield, H. Constraints on soluble aerosol iron flux to the Southern Ocean at the Last Glacial Maximum. *Nature communications* **6** (2015).

[28] Gu, S. *et al.* Reduced Antarctic Bottom Water overturning rate during the early last deglaciation inferred from radiocarbon records. *Nature Communications* **16**, 7777 (2025).

[29] Oppo, D. W., Curry, W. B. & McManus, J. F. What do benthic δ13c and δ18o data tell us about Atlantic circulation during Heinrich Stadial 1? *Paleoceanography* **30**, 353–368 (2015).

[30] Weaver, A. J. *et al.* The UVic Earth System Climate model: Model description, climatology, and applications to past, present and future climates. *Atmosphere-Ocean* **39**, 361–428 (2001).

[31] Wilmes, S.-B., Schmittner, A. & Green, J. Glacial ice sheet extent effects on modeled tidal mixing and the global overturning circulation. *Paleoceanography and Paleoclimatology* **34**, 1437–1454 (2019).

[32] Schmittner, A. Southern ocean sea ice and radiocarbon ages of glacial bottom waters. *Earth and Planetary Science Letters* **213**, 53–62 (2003).

[33] Meissner, K., Weaver, A., Matthews, H. & Cox, P. The role of land surface dynamics in glacial inception: a study with the Uvic Earth System Model. *Climate Dynamics* **21**, 515–537 (2003).

[34] Somes, C. J. & Oschlies, A. On the influence of "non-redfield" dissolved organic nutrient dynamics on the spatial distribution of n2 fixation and the size of the marine fixed nitrogen inventory. *Global Biogeochemical Cycles* **29**, 973–993 (2015).

[35] Kvale, K. *et al.* Explicit silicate cycling in the Kiel Marine Biogeochemistry Model version 3 (KMBM3) embedded in the UVic ESCM version 2.9. *Geoscientific Model Development* **14**, 7255–7285 (2021).

[36] Somes, C. J. *et al.* Constraining global marine iron sources and ligand-mediated scavenging fluxes with GEOTRACES dissolved iron measurements in an ocean biogeochemical model. *Global Biogeochemical Cycles* **35**, e2021GB006948 (2021).

[37] Peltier, W., Argus, D. & Drummond, R. Space geodesy constrains ice age terminal deglaciation: The global ice-6g_c (vm5a) model. *Journal of Geophysical Research: Solid Earth* **120**, 450–487 (2015).

[38] Muglia, J. & Schmittner, A. Carbon isotope constraints on glacial Atlantic meridional overturning: Strength vs depth. *Quaternary Science Reviews* **257**, 106844 (2021).

[39] Sigman, D. M., De Boer, A. M. & Haug, G. H. Antarctic stratification, atmospheric water vapor, and heinrich events: A hypothesis for late pleistocene deglaciations. *Ocean Circulation: Mechanisms and Impacts-Past and Future*

Changes of Meridional Overturning 335–349 (2007).

[40] Braconnot, P. *et al.* Evaluation of climate models using palaeoclimatic data. *Nature Climate Change* **2**, 417 (2012).

[41] Muglia, J., Somes, C. J., Nickelsen, L. & Schmittner, A. Combined effects of atmospheric and seafloor iron fluxes to the glacial ocean. *Paleoceanography* **32**, 1204–1218 (2017).

[42] Lambert, F. *et al.* Dust fluxes and iron fertilization in Holocene and Last Glacial Maximum climates. *Geophysical Research Letters* **42**, 6014–6023 (2015).

[43] Gebbie, G. How much did glacial north Atlantic water shoal? *Paleoceanography* **29**, 190–209 (2014).

[44] Schmittner, A. *et al.* Calibration of the carbon isotope composition (δ13c) of benthic foraminifera. *Paleoceanography* **32**, 512–530 (2017).

[45] Snoll, B., Ivanovic, R. F., Valdes, P. J., Maycock, A. C. & Gregoire, L. J. Effect of orographic gravity wave drag on Northern Hemisphere climate in transient simulations of the last deglaciation. *Climate Dynamics* **59**, 2067–2079 (2022).

[46] Ivanovic, R. *et al.* Acceleration of northern ice sheet melt induces AMOC slowdown and northern cooling in simulations of the early last deglaciation. *Paleoceanography and Paleoclimatology* **33**, 807–824 (2018).

[47] Sime, L. C. *et al.* Sea ice led to poleward-shifted winds at the Last Glacial Maximum: The influence of state dependency on CMIP5 and PMIP3 models. *Climate of the Past* **12**, 2241–2253 (2016).

[48] Menviel, L. *et al.* Poorly ventilated deep ocean at the Last Glacial Maximum inferred from carbon isotopes: A data-model comparison study. *Paleoceanography* **32**, 2–17 (2017).

[49] Gu, S. *et al.* Assessing the potential capability of reconstructing glacial Atlantic water masses and AMOC using multiple proxies in CESM. *Earth and Planetary Science Letters* **541**, 116294 (2020).

Supplementary Meterials for Southern Ocean ventilation sets up deglacial deep ocean configuration and CO_2 rise

Juan Muglia[1,2*], Andreas Schmittner[3], Stefan Mulitza[4], Patrick A. Rafter[5], Janne Repschläger[6], Christopher Somes[7], Sophie-Berenice Wilmes[8]

[1*]Centro para el Estudio de los Sistemas Marinos, CONICET, Bv. Almte Brown 2915, Puerto Madryn, 9120, Chubut, Argentina.
[2*]Universidad Nacional de la Patagonia San Juan Bosco, Bv. Almte Brown 3051, Puerto Madryn, 9120, Chubut, Argentina.
[3]College of Earth, Ocean, and Atmospheric Sciences, Oregon State University, 101 SW 26th St, Corvallis, 97331, Oregon, USA.
[4]MARUM - Center for Marine Environmental Sciences, University of Bremen, Leobener Str. 8, Bremen, 28359, Germany.
[5]College of Marine Science, University of South Florida, 830 1st St S, St. Petersburg, 33701, Florida, USA.
[6]Department of Climate Geochemistry, Max Planck Institute for Chemistry, Hahn-Meitner Weg 1, Mainz, 55128, Germany.
[7]GEOMAR Helmholtz Centre for Ocean Research, Wischhofstr. 1-3, Kiel, 24148, Germany.
[8]School of Ocean Sciences, University of Bangor, Menai Bridge LL59 5AB, Bangor, UK.

*Corresponding author(s). E-mail(s): jmuglia@cenpat-conicet.gob.ar;

Table S1 Model-data R and RMSE for benthic minus atmospheric radiocarbon ages from a subset of our simulations and a global data compilation[1]. The subset was chosen to focus the analysis on the physical effects on radiocarbon ages.

Simulation	R	RMSE (^{14}C a)
Control	0.56	574
Ldust	0.63	483
SOWind	0.66	448
SOWind_Ldust	0.69	385
LFWF	0.54	658
HFWF	0.60	602
LFWF_SOWind_Ldust	0.68	455
HFWF_SOWind_Ldust	0.67	469

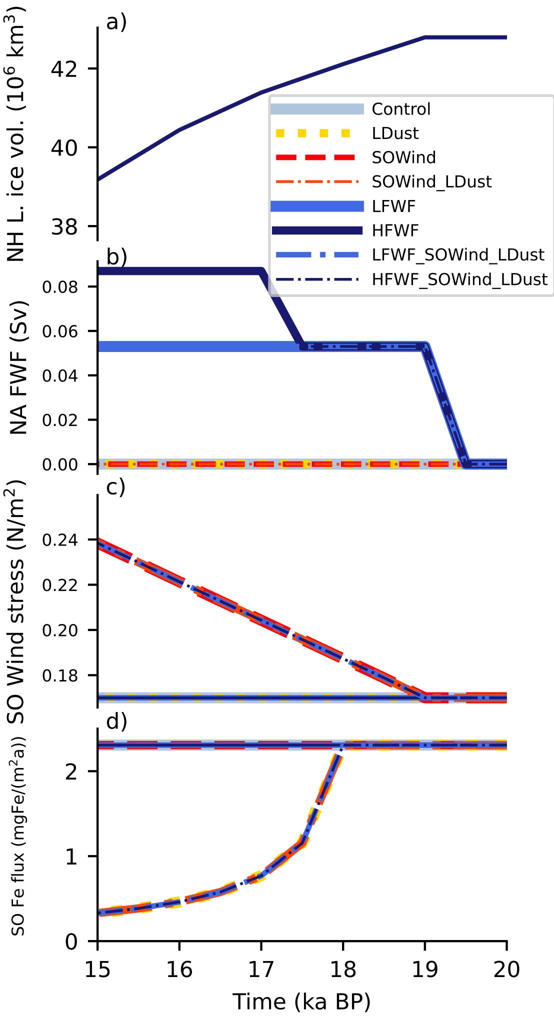

Fig. S1 Main transient forcings applied to our simulations. (a) Northern Hemisphere land ice sheet volume, (b) North Atlantic Fresh Water Fluxes, (c) Southern Ocean zonal wind stress, (d) Southern Ocean atmospheric iron flux.

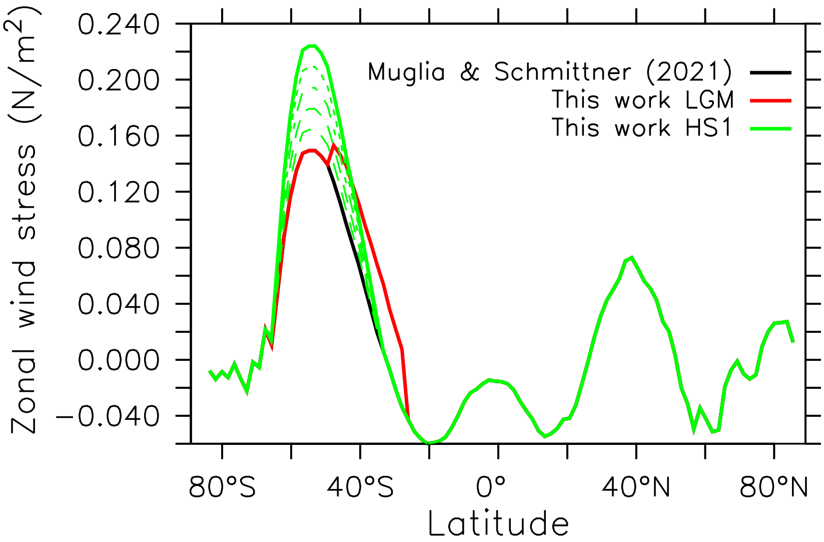

Fig. S2 Zonally-averaged zonal wind stress applied in our simulations. The red curve corresponds to the field used in our LGM initial condition simulation. The green solid curve corresponds to the field used in the final state (15 ka) of **SOWind**, **SOWind_Ldust**, **LowFWF_SOWind_Ldust**, and **HighFWF_SOWind_Ldust** simulations. The dashed green curves correspond to the transition fields from 20 to 15 ka. **Weak_SOWind_LDust** deglacial simulation. The black curve corresponds to the field used in LGM simulations of Muglia and Schmittner (2021)[2].

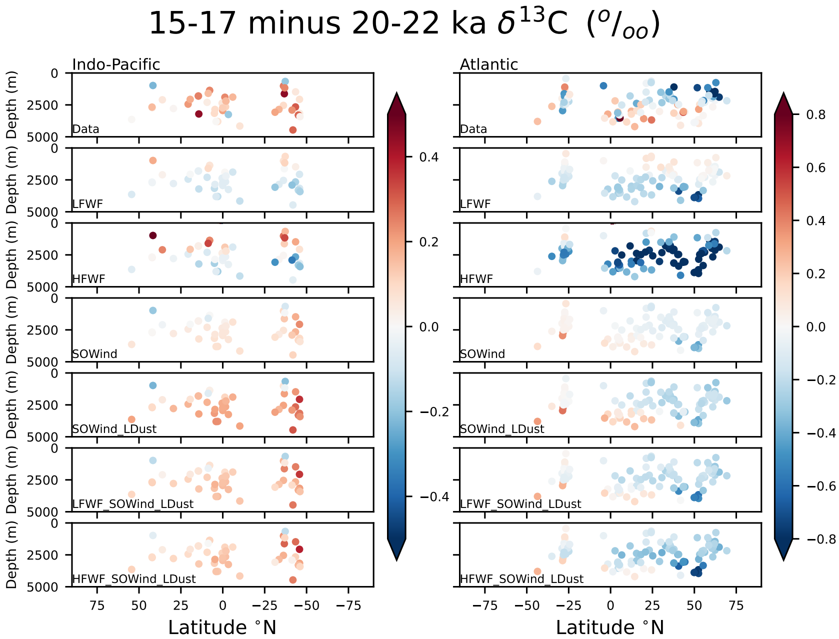

Fig. S3 Section plots of zonally-collapsed (left) Indo-Pacific and (right) Atlantic δ^{13}C differences between HS1 and LGM time slices in the data[3] and our simulations, as indicated. Model output was extracted at the data locations.

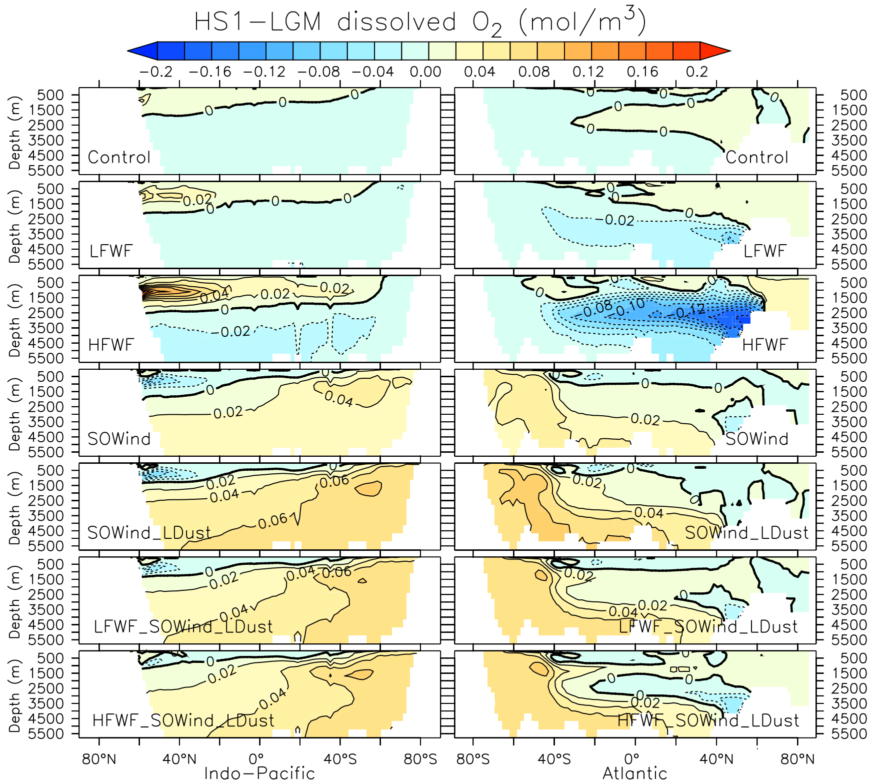

Fig. S4 Zonally-averaged dissolved O_2 difference between the 15-17 and 20-22 ka model intervals in our simulations, as indicated.

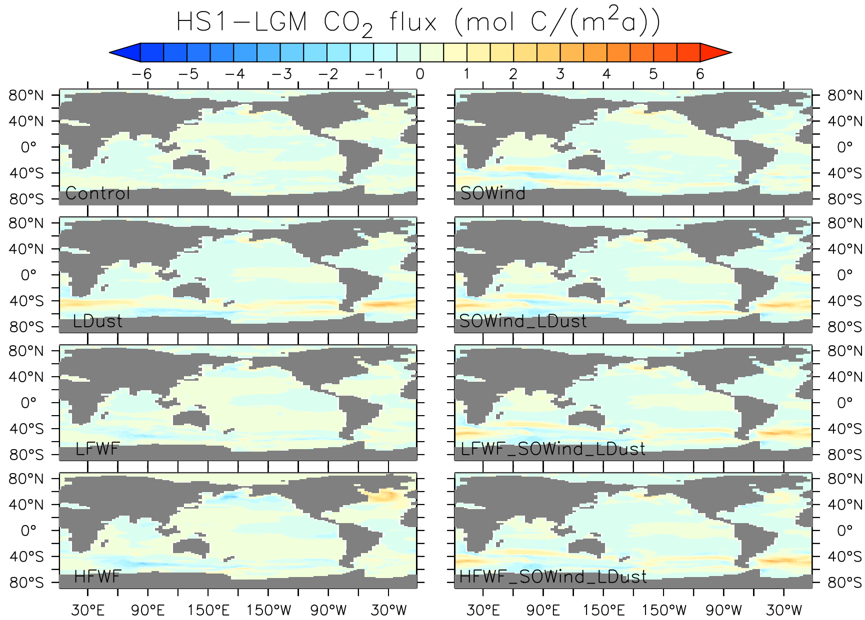

Fig. S5 Differences in upward carbon flux from the surface ocean to the atmosphere between 15-17 and 20-22 ka model intervals in our simulations.

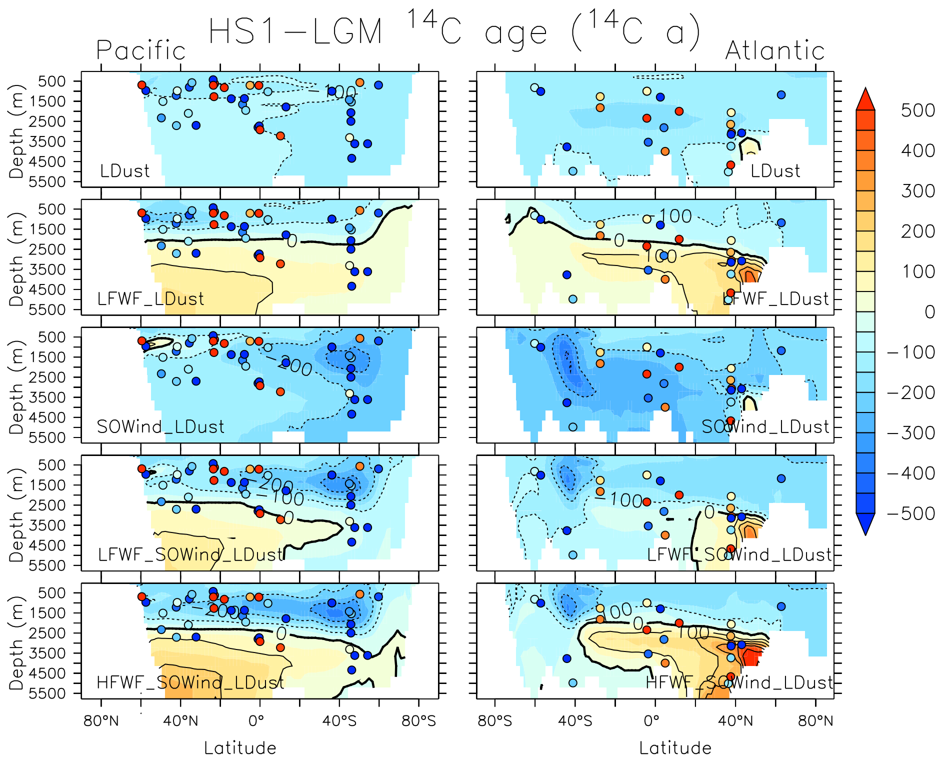

Fig. S6 Zonally-averaged radiocarbon age difference between the 15-17 and 20-22 ka model intervals in our simulations, as indicated. Overlayed are differences using the same time slices from a benthic foraminifera radiocarbon age data compilation[1].

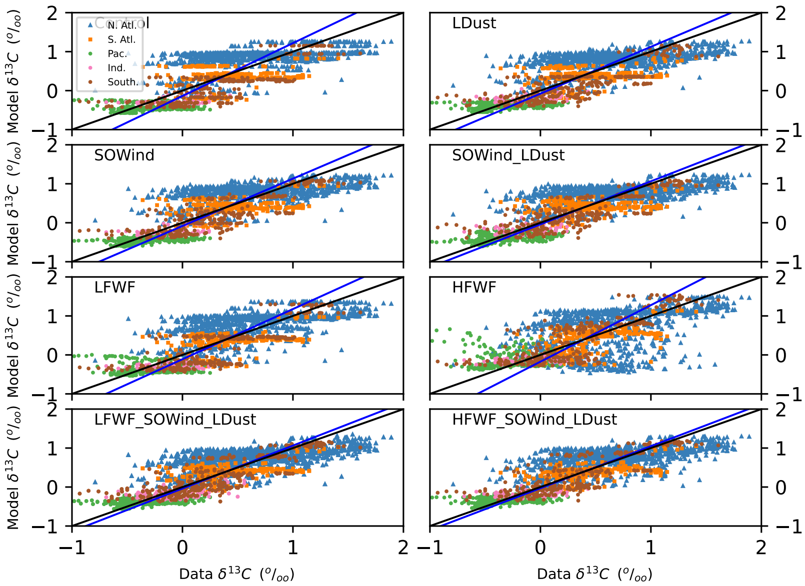

Fig. S7 δ^{13}C model versus data scatter plots for the 15-20 ka time interval. Black lines correspond to the 1:1 line. Blue lines correspond to the model versus data linear regression. Color and symbol codes represent different ocean basins. The slopes associated with the linear regressions are listed in Table 1. Offsets in global mean δ^{13}C between simulations and data were removed to produce the figure and calculate the linear fits.

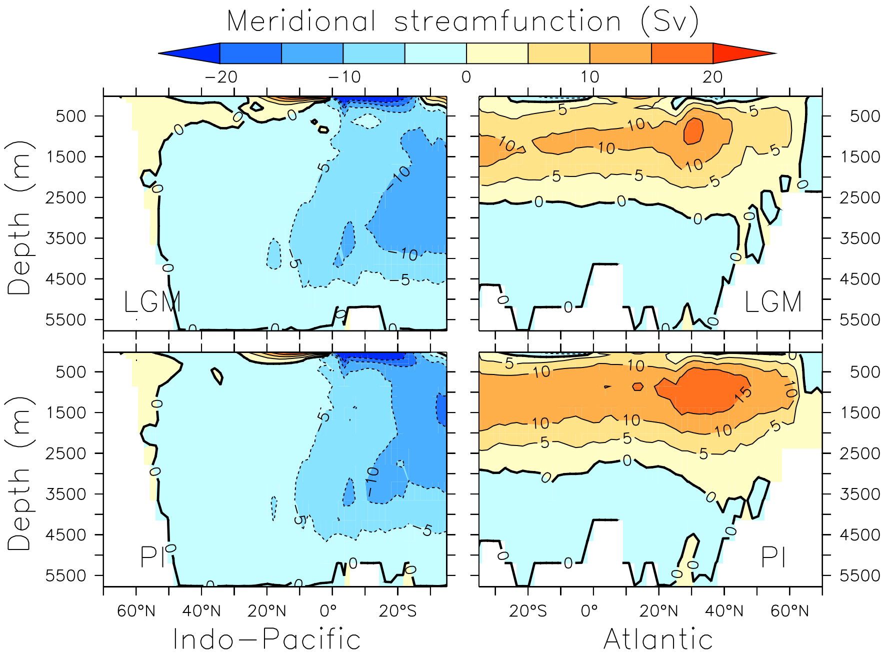

Fig. S8 Meridional streamfunction plots of our LGM initial condition and preindustrial simulations. Red(blue) colors indicate nortward(southward) overturning in the upper part of each cell as a function of latitude and depth. Ocean basins are indicated in the plot.

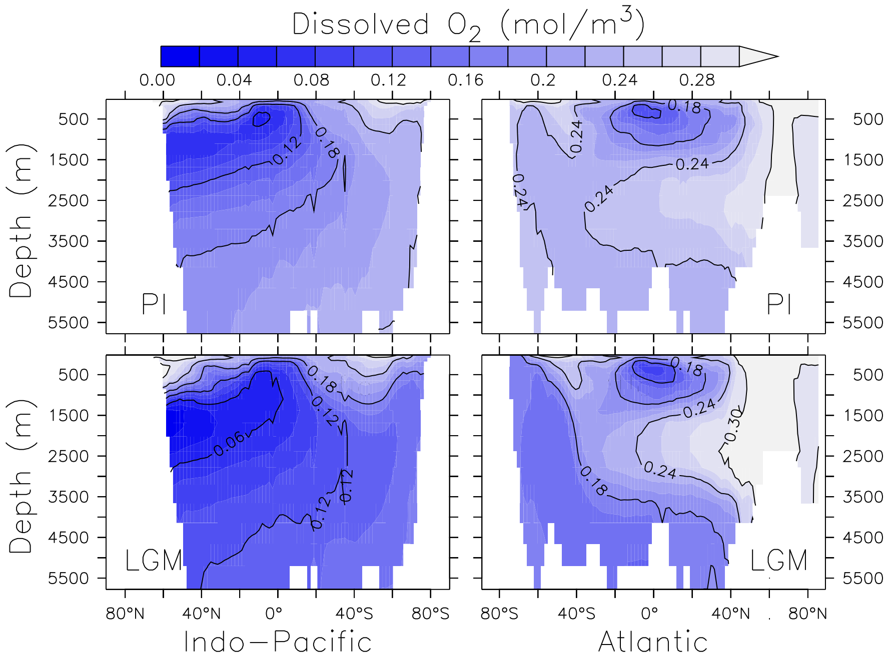

Fig. S9 Zonally-averaged dissolved O_2 in our (top) LGM initial condition and (bottom) preindustrial simulations. Ocean basins are indicated in the plot.

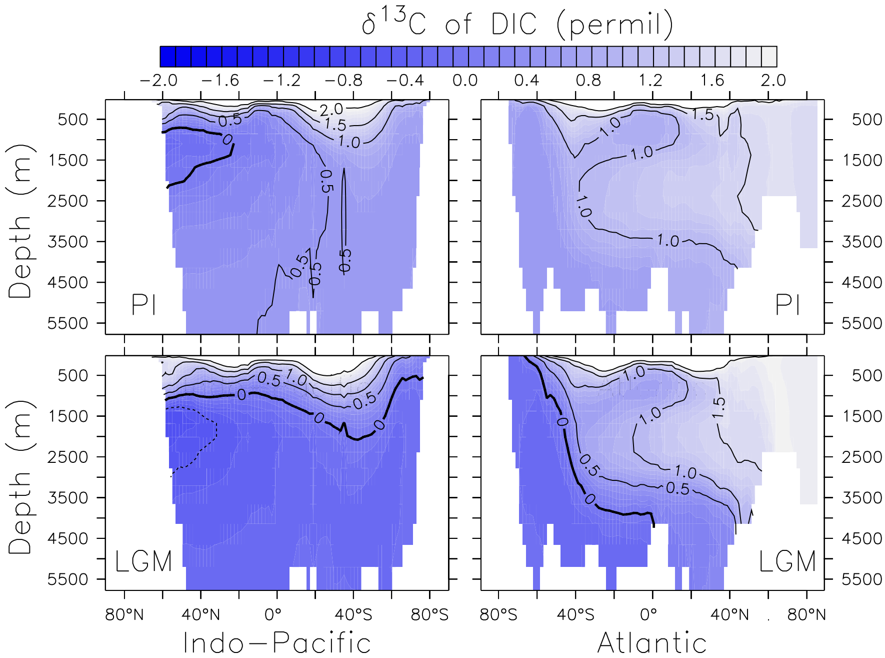

Fig. S10 As Fig. S9, but for δ^{13}C of DIC.

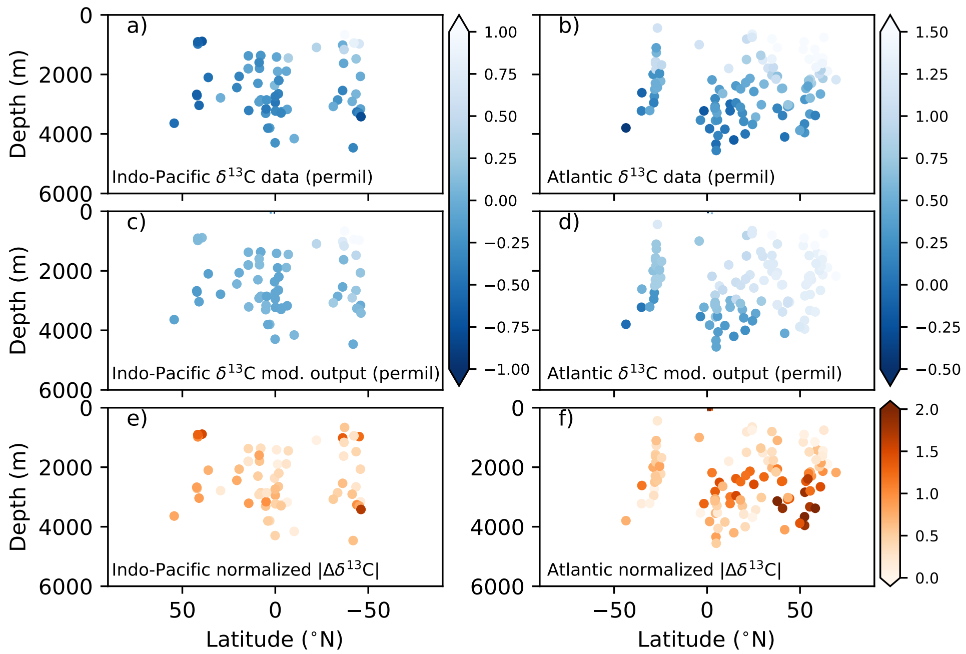

Fig. S11 (a-b) δ^{13}C of *C. wuellerstorfi* from a high-resolution, global database[3]. (c-d) δ^{13}C of DIC from our LGM initial condition simulation, transformed into *C. wuellerstorfi* δ^{13}C as described in the Methods section, at model grid boxes co-located with coring site positions of the database. (e-f) Absolute value of difference between model and data δ^{13}C, normalized by the combined model and data LGM minus Late Holocene global δ^{13}C difference (0.54 permil)

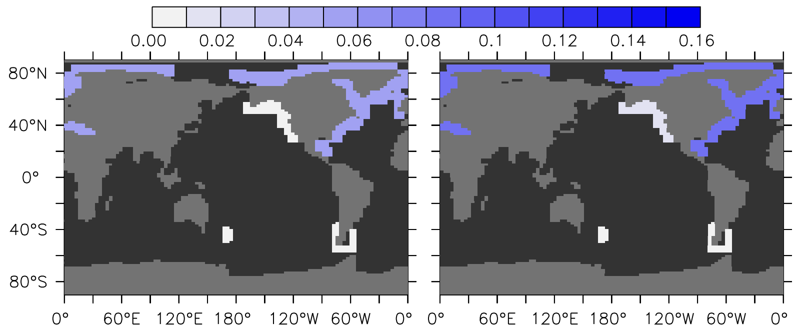

Fig. S12 Fresh water fluxes applied in some of our deglacial simulations. (left) Fluxes used in the **LFWF** and **LFWF_SOWind_Ldust** experiments between 20 and 15 ka, and in the **HFWF** and **HFWF_SOWind_Ldust** experiments between 20 and 17 ka. (right) Fluxes used in the **HFWF** and **HFWF_SOWind_Ldust** experiments between 17 and 15 ka.

References

[1] Rafter, P. A. *et al.* Global reorganization of deep-sea circulation and carbon storage after the last ice age. *Science Advances* **8**, eabq5434 (2022).

[2] Muglia, J. & Schmittner, A. Carbon isotope constraints on glacial Atlantic meridional overturning: Strength vs depth. *Quaternary Science Reviews* **257**, 106844 (2021).

[3] Muglia, J. *et al.* A global synthesis of high-resolution stable isotope data from benthic foraminifera of the last deglaciation. *Scientific Data* **10**, 131 (2023).